

Simulating the dynamics of relativistic stars via a light-cone approach

Florian Siebel¹, José A. Font^{1,2}, Ewald Müller¹, Philippos Papadopoulos³

⁽¹⁾ *Max-Planck-Institut für Astrophysik, Karl-Schwarzschild-Str. 1, D-85741 Garching, Germany*

⁽²⁾ *Departamento de Astronomía y Astrofísica, Universidad de Valencia, 46100 Burjassot (Valencia), Spain*

⁽³⁾ *School of Computer Science and Mathematics,
University of Portsmouth, Portsmouth, PO1 2EG, UK*

(Dated: October 25, 2018)

We present new numerical algorithms for the coupled Einstein-perfect fluid system in axisymmetry. Our framework uses a foliation based on a family of light cones, emanating from a regular center, and terminating at future null infinity. This coordinate system is well adapted to the study of the dynamical spacetimes associated with isolated relativistic compact objects such as neutron stars. In particular, the approach allows the unambiguous extraction of gravitational waves at future null infinity and avoids spurious outer boundary reflections. The code can accurately maintain long-term stability of polytropic equilibrium models of relativistic stars. We demonstrate global energy conservation in a strongly perturbed neutron star spacetime, for which the total energy radiated away by gravitational waves corresponds to a significant fraction of the Bondi mass. As a first application we present results in the study of pulsations of axisymmetric relativistic stars, extracting the frequencies of the different fluid modes in fully relativistic evolutions of the Einstein-perfect fluid system and making a first comparison between the gravitational news function and the predicted wave using the approximations of the quadrupole formula.

PACS numbers: 04.25.Dm, 04.40.-b, 95.30.Lz, 04.40.Dg

I. INTRODUCTION

The dynamics of relativistic compact objects is of interest both to the astrophysical and relativity communities. These objects represent on the one hand systems that may be active in stellar collapse, central engines for Gamma Ray Bursts, and are potentially strong sources of gravitational radiation. On the other hand, they represent non-trivial solutions to the Einstein equations, possibly exhibiting directly the predictions of that theory for cosmic censorship and black hole formation.

Despite the obvious interest in building a reliable spacetime description of such systems, the process has been marred with difficulties [1, 2]. One of the central problems concerns the formulation and solution of the initial value problem for the Einstein equations, a research effort that is still largely ongoing. The numerical relativist must overcome a daunting list of problems, including a long term stable formulation of the initial value problem, the preservation of the constraints, the consistent imposition of boundary conditions and the reliable extraction of physical information (including gravitational waveforms).

We propose that for a wide and interesting class of spacetimes most of the above concerns can be successfully dealt with by the use of a characteristic initial value formulation for the Einstein equations. In particular we argue that the study of the non-linear dynamics of isolated relativistic stars is optimally performed within this framework and we proceed to illustrate the technical procedures that support this claim.

The incorporation of matter fields in the characteristic formulation of the Einstein equation was considered as early as 1983 [3] but the successful integration of the

coupled system had to wait for the development of stable algorithms for the *vacuum* Einstein problem. One dimensional schemes were developed in [4]. Algorithms for axisymmetric spacetimes, notably including a regular origin, were presented in [5]. Recently using similar techniques, axisymmetric vacuum black hole spacetimes have been evolved [6]. Techniques for extending finite difference algorithms to 3D were presented in [7]. Three dimensional codes excluding the origin of the light cones (hence presently unsuitable for stellar collapse studies) were presented in [8]. For an alternative approach see [9].

With reliable algorithms for the vacuum Einstein equations available, a new line of research for the incorporation of relativistic hydrodynamics into numerical relativity was initiated recently [10]. This approach brings into the considerations the modern machinery from Computational Fluid Mechanics. In this procedure, the evolution equations for the matter fields are solved using relativistic high-resolution shock-capturing (HRSC) schemes [10, 11] based upon (exact or approximate) Riemann solvers. A general formalism has been developed, which is now being systematically applied to problems of increasing complexity. Applications in spherical symmetry have already been presented in the literature: investigations of accreting dynamic black holes can be found in [10, 12]. Studies of the gravitational collapse of supermassive stars are discussed in [13] and studies of the interaction of scalar fields with relativistic stars are presented in [14]. We note that there has been already a proof-of-principle demonstration of the inclusion of matter fields in three dimensions [15].

In this paper we apply the general framework laid out in [10] in the context of axisymmetric neutron star spacetimes. The code we have developed has been built upon previous work by Gómez, Papadopoulos and Winicour [5], who constructed an axisymmetric character-

istic *vacuum* code. The numerical implementation of the field equations of general relativity is based on the light cone formalism of Bondi [16, 17] and Tamburino-Winicour [18].

The broad target of this project is the investigation of relativistic stellar dynamics (including collapse) using numerical relativity. A prerequisite for such studies is the development of very accurate and long-term stable general relativistic codes. It would seem that the feature list of the characteristic approach makes it ideal for such studies. One serious bottleneck of the approach is the breakdown of a lightlike coordinate system in the emergence of light caustics. Interestingly though, due to its quasi-spherical nature, no matter how agitated a relativistic core, it is unlikely to focus the light cones emanating from its interior.

The light cone approach has a number of advantages compared to spacelike foliations: i) It is physically motivated; the light cones offer a simple and unambiguous physical gauge on which to base the numerical spacetime grid. ii) It is unconstrained; the evolved variables capture rather directly the true degrees of freedom of the gravitational field. iii) It is very efficient; even in 3D, there are but two partial differential equations to solve, along with a set of radial integrations along the light cones. iv) It allows for well defined compactification [19] of the domain, which leads to perfect outer boundary conditions. v) Finally, and perhaps most importantly, the above theoretical advantages have been shown in a series of works to translate to remarkably numerically robust and stable codes (see e.g. [20]). For a recent review of the approach the reader is referred to [21].

An important focus of research in numerical relativity has been the investigation of dynamical spacetimes of relativistic stars. While the pioneer investigations were mostly concerned with the study of spherically-symmetric gravitational collapse scenarios the effort is nowadays expanding to the study of the merging of compact neutron star binaries. Advances in the numerical formulation of the equations as well as in computational power have made possible to transform the numerical evolution of neutron stars in general relativity into an active field of research [22, 23, 24, 25, 26].

The paper is organized as follows: In Sec. II we describe our mathematical framework for characteristic numerical relativity in axisymmetry. The next section describes our numerical implementation in some detail. In Sec. IV we present tests to assess the validity of the different regimes of our numerical implementation. In Sec. V we apply the current code in studies of stellar pulsations. The last section concludes with a short summary.

II. MATHEMATICAL FRAMEWORK

We will work with the coupled system of Einstein and relativistic perfect fluid equations

$$G_{ab} = \kappa T_{ab}, \quad (1)$$

$$\nabla_a T^{ab} = 0, \quad (2)$$

$$\nabla_a(\rho u^a) = 0, \quad (3)$$

with the latter two equations being the local conservation laws of stress-energy and current density. The energy-momentum tensor T_{ab} has the form

$$T_{ab} = \rho h u_a u_b + p g_{ab}. \quad (4)$$

In this expression ρ denotes the rest mass density, $h = 1 + \epsilon + \frac{p}{\rho}$ is the specific enthalpy, ϵ is the specific internal energy and p is the pressure of the fluid. The four-vector u^a , the 4-velocity of the fluid, fulfills the normalization condition $g_{ab}u^a u^b = -1$. Using geometrized units ($c = G = 1$) the coupling constant is $\kappa = 8\pi$. In order to close the system of fluid equations, an equation of state (EoS) has also to be prescribed, $p = p(\rho, \epsilon)$.

A. The Einstein equations for the Bondi metric

As a geometric and coordinate framework we will use the Bondi (radiative) metric [16] to describe the spacetime

$$ds^2 = - \left(\frac{V}{r} e^{2\beta} - U^2 r^2 e^{2\gamma} \right) du^2 - 2e^{2\beta} du dr - 2Ur^2 e^{2\gamma} du d\theta + r^2 (e^{2\gamma} d\theta^2 + e^{-2\gamma} \sin^2 \theta d\phi^2), \quad (5)$$

with coordinates $(x^0, x^1, x^2, x^3) = (u, r, \theta, \phi)$, where u is a null coordinate labeling outgoing light-cones, r is the radial coordinate whose level surfaces (two-spheres) have area $4\pi r^2$, and θ and ϕ are angular coordinates with ϕ being a Killing coordinate. The metric functions V , U , β and γ depend on the coordinates u , r and θ . We choose the origin of the coordinate system $r = 0$ to lie on the axis of our axisymmetric stellar configurations. With the above assumptions, the gravitational field equations read explicitly

$$R_{ab} = \kappa \left(\rho h (u_a u_b + \frac{1}{2} g_{ab}) - p g_{ab} \right), \quad (6)$$

where the relevant components of the Ricci tensor R_{ab} are

$$\frac{r}{4}R_{rr} = \beta_{,r} - \frac{r}{2}(\gamma_{,r})^2, \quad (7)$$

$$2r^2R_{r\theta} = (r^4e^{2(\gamma-\beta)}U_{,r})_{,r} - 2r^2(\beta_{,r\theta} - \gamma_{,r\theta} + 2\gamma_{,r}\gamma_{,\theta} - \frac{2}{r}\beta_{,\theta} - 2\gamma_{,r}\cot\theta), \quad (8)$$

$$-r^2e^{2\beta}g^{AB}R_{AB} = 2V_{,r} + \frac{1}{2}r^4e^{2(\gamma-\beta)}(U_{,r})^2 - r^2U_{,r\theta} - 4rU_{,\theta} - r^2U_{,r}\cot\theta - 4rU\cot\theta \\ + 2e^{2(\beta-\gamma)}\{-1 - (3\gamma_{,\theta} - \beta_{,\theta})\cot\theta - \gamma_{,\theta\theta} + \beta_{,\theta\theta} + (\beta_{,\theta})^2 + 2\gamma_{,\theta}(\gamma_{,\theta} - \beta_{,\theta})\}, \quad (9)$$

$$-r^2e^{2\beta}g^{\phi\phi}R_{\phi\phi} = 2r(r\gamma)_{,ur} + (1 - r\gamma_{,r})V_{,r} - (r\gamma_{,rr} + \gamma_{,r})V - r(1 - r\gamma_{,r})U_{,\theta} - r^2(\cot\theta - \gamma_{,\theta})U_{,r} \\ + e^{2(\beta-\gamma)}(-1 - (3\gamma_{,\theta} - 2\beta_{,\theta})\cot\theta - \gamma_{,\theta\theta} + 2\gamma_{,\theta}(\gamma_{,\theta} - \beta_{,\theta})) \\ + rU(2r\gamma_{,r\theta} + 2\gamma_{,\theta} + r\gamma_{,r}\cot\theta - 3\cot\theta). \quad (10)$$

In Eq. (9) A, B denote the angular coordinates, $A, B = 2, 3$. As usual a comma is used to denote a partial derivative.

The Einstein equations decompose into hypersurface equations, evolution equations and conservation laws. The hypersurface equations, Eqs. (7)-(9), form a hierarchical set for $\beta_{,r}$, $U_{,r}$ and $V_{,r}$. The evolution equation is an expression for $(r\gamma)_{,ur}$ given by Eq. (10). The light-cone problem is formulated in the region of spacetime between a timelike worldtube Γ , which in our case is located at the origin of the radial coordinate $r = 0$, and future null infinity \mathcal{J}^+ . Initial data γ is prescribed on an initial light cone $u = 0$ in this domain. Boundary data for β , U , V and γ is also required on Γ .

As shown in the original paper of Bondi [16], the contracted Bianchi identities for the vacuum field equations enforce all other Ricci tensor components to vanish, if they vanish on a worldline. In the same way one can show, that the contracted Bianchi identities for the matter system enforce all other components of the Einstein equation (6) (see [3]).

The reformulation of the above form of the equations for numerical integrations follows the work of Ref. [5]. First, in order to be able to compactify the entire spacetime and to better resolve interesting parts of the numerical integration (e.g. a stellar configuration centered at $r = 0$) we allow, starting from a radial coordinate $x \in [0, 1]$, for a coordinate transformation of the radial

coordinate $x \rightarrow r(x)$, with an associated derivative

$$dx/dr = f^2(x). \quad (11)$$

This transformation generalizes the results of [5], where the fixed grid $r(x) = x/(1 - x)$ was used. Furthermore, in order to eliminate singular terms at the poles we use the new coordinate [27]

$$y = -\cos\theta \quad (12)$$

and we introduce the new variables

$$S = \frac{V - r}{r^2}, \quad (13)$$

$$\hat{U} = \frac{U}{\sin\theta}, \quad (14)$$

$$\hat{\gamma} = \frac{\gamma}{\sin^2\theta}. \quad (15)$$

The metric, hence, takes the form

$$ds^2 = \left(-\frac{V}{r}e^{2\beta} + U^2r^2e^{2\gamma}\right)du^2 - 2f^{-2}e^{2\beta}dudx \\ - 2\hat{U}r^2e^{2\gamma}dudy + r^2(e^{2\gamma}\sin^{-2}\theta dy^2 \\ + e^{-2\gamma}\sin^2\theta d\phi^2). \quad (16)$$

The hypersurface equations (7)-(9) thus read

$$\beta_{,x} = \frac{r}{2}f^2\bar{y}^2(\hat{\gamma}_{,x})^2 + \frac{r}{4}f^2R_{xx}, \quad (17)$$

$$\left(r^4f^2e^{2(\hat{\gamma}\bar{y}-\beta)}\hat{U}_{,x}\right)_{,x} = 2r^2\left\{\beta_{,xy} - \frac{2}{rf^2}\beta_{,y} + 4y\hat{\gamma}_{,x} + \bar{y}[2\hat{\gamma}_{,x}(\bar{y}\hat{\gamma}_{,y} - 2y\hat{\gamma}) - \hat{\gamma}_{,xy}]\right\} + 2r^2R_{xy}, \quad (18)$$

$$r^2f^2S_{,x} + 2rS = -1 - 4ry\hat{U} - r^2f^2y\hat{U}_{,x} + 2r\bar{y}\hat{U}_{,y} + \bar{y}\left(\frac{r^2}{2}f^2\hat{U}_{,xy} - \frac{r^4}{4}f^4e^{2(\hat{\gamma}\bar{y}-\beta)}(\hat{U}_{,x})^2\right) \\ - e^{2(\beta-\hat{\gamma}\bar{y})}\{-1 - 12\hat{\gamma} - 2y\beta_{,y} + \bar{y}[10\hat{\gamma} + 8y\hat{\gamma}_{,y} + 8\hat{\gamma}^2 + 4y\hat{\gamma}\beta_{,y} + \beta_{,yy} + (\beta_{,y})^2] \\ - \bar{y}^2[8\hat{\gamma}^2 + 2\hat{\gamma}_{,y}\beta_{,y} + \hat{\gamma}_{,yy} + 8y\hat{\gamma}\hat{\gamma}_{,y}] + 2\bar{y}^3\hat{\gamma}_{,y}^2\} - \frac{r^2}{2}e^{2\beta}g^{AB}R_{AB}. \quad (19)$$

We have used here the notation $\bar{y} = 1 - y^2$ and $(\cdot)_{,x}$ and $(\cdot)_{,y}$ to denote the partial derivatives with respect to x and y , in contrast to the partial derivatives with respect to r and θ . Note, that the Ricci tensor components are those in x, y -coordinates.

Due to this choice of variables, the Einstein equations are non-singular on the polar axis, where $y = \pm 1$. Note, that the y -component of the four-velocity fulfills

$$u_y = \frac{u_\theta}{\sin \theta}, \quad (20) \quad \text{i.e. explicitly}$$

which is in analogy to Eq. (14).

The evolution equation for $\hat{\gamma}$ is written in the form of a wave equation for the quantity $\hat{\psi}$

$$\hat{\psi} = r\hat{\gamma}, \quad (21) \quad \text{and}$$

$$\tilde{g}^{ab}\tilde{\nabla}_a\tilde{\nabla}_b\hat{\psi} = -e^{-2\beta}\hat{H}, \quad (22)$$

where the $\tilde{\cdot}$ quantities are induced by the 2-metric

$$d\sigma^2 = -\frac{V}{r}e^{2\beta}du^2 - 2e^{2\beta}du\,dr, \quad (23)$$

$$\tilde{g}^{ab}\tilde{\nabla}_a\tilde{\nabla}_b\hat{\psi} = -e^{-2\beta}(2\hat{\psi}_{ur} - (\frac{V}{r}\hat{\psi}_{,r})_{,r}), \quad (24)$$

$$\begin{aligned} \hat{H} = & -\frac{r}{2}f^2\hat{U}_{,xy} - \hat{U}_{,y} - rf^2\hat{\gamma}_{,x}\hat{U}_{,y}\bar{y} + \frac{r^3}{4}f^4e^{2(\hat{\gamma}\bar{y}-\beta)}(\hat{U}_{,x})^2 \\ & - (S + rf^2S_{,x})\hat{\gamma} + \frac{1}{r}e^{2(\beta-\hat{\gamma}\bar{y})}(\beta_{,yy} + (\beta_{,y})^2) + 4\hat{\gamma}\hat{U}_y \\ & + 2rf^2\hat{\gamma}\hat{U}_{,xy} + 6rf^2\hat{\gamma}_{,x}\hat{U}_y - \bar{y}\left(rf^2\hat{\gamma}_{,y}\hat{U}_{,x} + 2rf^2\hat{\gamma}_{,xy}\hat{U} + 2\hat{\gamma}_{,y}\hat{U}\right) \\ & + \frac{1}{2r}e^{2(\beta-\hat{\gamma}\bar{y})}\kappa\rho hu_y u_y. \end{aligned} \quad (25)$$

B. The relativistic perfect fluid equations

Whereas Eq. (3) is a strict conservation law, Eq. (2) involves source terms when writing the covariant derivatives in terms of partial derivatives. In the presence of a Killing vector field it can be recast as a conservation law. Following [28], the number of source terms in Eq. (2) is minimized using the equivalent form

$$\nabla_a T^a_b = 0. \quad (26)$$

In our hydrodynamics code we use the form given by Eq. (2) in order to set up the evolution equation for the radial momentum. This is motivated by stability considerations when evolving spherical neutron star models (see below). However, to set up the evolution equation for the polar component of the momentum we use Eq. (26). This form of the conservation law eliminates singular behavior of the y -component of the velocity at the polar axis.

After introducing the definitions $U^0 = \sqrt{-g}T^{00}$, $U^x = \sqrt{-g}T^{0x}$, $U_y = \sqrt{-g}T^0_y$ and $U^4 = \sqrt{-g}\rho u^0$, the fluid equations can be cast into a first-order flux-conservative, hyperbolic system for the state-vector $\mathbf{U} = (U^0, U^x, U_y, U^4)$

$$\partial_0 U^0 + \partial_j F^{j0} = S^0, \quad (27)$$

$$\partial_0 U^x + \partial_j F^{jx} = S^x, \quad (28)$$

$$\partial_0 U_y + \partial_j F^j_y = S_y, \quad (29)$$

$$\partial_0 U^4 + \partial_j F^{j4} = S^4. \quad (30)$$

The flux vectors are defined as

$$F^{j0} = \sqrt{-g} T^{j0}, \quad (31)$$

$$F^{jx} = \sqrt{-g} T^{jx}, \quad (32)$$

$$F^j_y = \sqrt{-g} T^j_y, \quad (33)$$

$$F^{j4} = \sqrt{-g} \rho u^j, \quad (34)$$

and the corresponding source terms read

$$S^a = g^{ab} S_b + \sqrt{-g} T^c_b \partial_c g^{ab}, \quad (35)$$

$$\begin{aligned} S_a &= \sqrt{-g} T^b_c \Gamma^c_{ab} \\ &= -\frac{\sqrt{-g}}{2} \rho h u_c u_d (g^{cd})_{,a} + p(\sqrt{-g})_{,a}, \end{aligned} \quad (36)$$

$$S^4 = 0, \quad (37)$$

In the above expressions $\sqrt{-g}$ is square root of the four dimensional metric determinant and Γ^a_{bc} are the Christoffel symbols.

C. Gravitational waves at null infinity

Using a compactified coordinate $x \in [0, 1]$, $\lim_{x \rightarrow 1} r(x) = \infty$, we have future null infinity \mathcal{J}^+ on our

grid, where we can unambiguously extract waveforms. Hence our approach does not suffer from the problem most numerical relativity codes have to deal with, i.e. extracting approximate gravitational waveforms at a finite distance (for a comparison, see [29, 30]). Performing a power series expansion of γ around future null infinity in inverse powers of the radial coordinate r

$$\gamma = K + \frac{c}{r} + O(r^{-2}), \quad (38)$$

the hypersurface equations (7)-(9) yield an expansion [3]

$$\beta = H + O(r^{-2}), \quad (39)$$

$$U = L + O(r^{-1}), \quad (40)$$

$$V = r^2(L \sin \theta)_{,\theta} / \sin \theta + r e^{2(H-K)} [1 + K_{,\theta\theta} + 2(H_{,\theta} \sin \theta)_{,\theta} / \sin \theta + 3K_{,\theta} \cot \theta + 4(H_{,\theta})^2 - 4H_{,\theta} K_{,\theta} - 2(K_{,\theta})^2] - 2e^{2H} M + O(r^{-1}), \quad (41)$$

where $M = M(\theta)$ denotes the Bondi mass aspect. As its straightforward extraction at \mathcal{J}^+ will be spoilt by the leading, diverging terms in Eq. (41), we follow the procedure proposed in [31] to determine the Bondi mass of a numerical spacetime. We numerically solve the hypersurface equations for the new metric variables

$$2\tau = (1 - y^2)^{-1/2} r^3 e^{2(\gamma-\beta)} U_{,r} + 2r\beta_{,y} - r^2(1 - y^2)^{-1} e^{2\gamma} [(1 - y^2)e^{-2\gamma}]_{,ry}, \quad (42)$$

$$2\mu = -V + r^2[(1 - y^2)^{1/2} U]_{,y} + r^3 e^{2\beta} \left[\frac{1}{2r} (1 - y^2) e^{-2\gamma} \right]_{,yyr} + e^{2\beta} [(1 - y^2) e^{-2\gamma} \tau]_{,y}, \quad (43)$$

(see [31] for more details). The Bondi mass M_B can then be readily computed as

$$M_B = \frac{1}{4\pi} \int \omega^{-1} e^{-2H} \mu|_{x=1} \sin \theta \, d\theta \, d\phi, \quad (44)$$

where ω denotes the conformal factor relating the two-geometry

$$d\hat{s}^2 = e^{2K} d\theta^2 + \sin^2 \theta e^{-2K} d\phi^2 \quad (45)$$

to the two-geometry of a unit sphere

$$d\hat{s}_B^2 = d\theta_B^2 + \sin^2 \theta_B d\phi_B^2. \quad (46)$$

The total energy emitted by gravitational waves during the time interval $[u, u + du]$ in angular directions $[\theta, \theta + d\theta] \times [\phi, \phi + d\phi]$ is [3]

$$dE = \frac{1}{16\pi} \omega^{-1} e^{-2H} \left\{ 2c_{,u} + \frac{(\sin \theta \, c^2 \, L)_{,\theta}}{\sin \theta \, c} + e^{-2K} \omega \sin \theta \left[\frac{(e^{2H} \omega)_{,\theta}}{\omega^2 \sin \theta} \right]_{,\theta} \right\}^2 \sin \theta d\theta d\phi du. \quad (47)$$

The quantities K, c, H and L are read off from the metric variables at \mathcal{J}^+ , e.g. $c = -(r^2 f^2 \frac{d\gamma}{dx})|_{x=1}$ (our coordinate transformations $r = r(x)$ fulfill the requirement that $r^2 f^2$ is finite).

For the extraction of waveforms seen from a distant inertial observer, we have to transform our coordinate system to a Bondi coordinate system. Following [8] the Bondi coordinate time u_B is related to the retarded time u as

$$du = \frac{1}{\omega} e^{-2H} du_B, \quad (48)$$

whereas the angular Bondi coordinate $y_B = -\cos(\theta_B)$ can be calculated from

$$dy = \frac{1}{\omega^2} dy_B. \quad (49)$$

With the definition of the news function

$$N = \frac{1}{2} \frac{e^{-2H}}{\omega^2} \left\{ 2c_{,u} + \frac{(\sin \theta \, c^2 \, L)_{,\theta}}{\sin \theta \, c} + e^{-2K} \omega \sin \theta \left[\frac{(e^{2H} \omega)_{,\theta}}{\omega^2 \sin \theta} \right]_{,\theta} \right\}, \quad (50)$$

and after integrating over the angles $\phi = \phi_B$, one recovers the expression for the total energy radiated according to Bondi [16]

$$dE = \frac{1}{2} N^2 dy_B \, du_B. \quad (51)$$

This relation allows us to check global energy conservation

$$ec := M_B(u) - M_B(u=0) + \int_0^u \int_{-1}^1 dE = 0. \quad (52)$$

For the calculation of the Bondi mass, Eq. (44), as well as for the calculation of the Bondi news, Eq. (50), we have to determine the conformal factor ω

$$d\hat{s}_B^2 = \omega^2 d\hat{s}^2. \quad (53)$$

It can be shown that the coordinate $y_B = -\cos(\theta_B)$ reads

$$y_B(y) = \tanh \left(\frac{1}{2} \int_{-1}^y \frac{e^{2K} - 1}{1 - \tilde{y}^2} d\tilde{y} + \frac{1}{2} \int_1^y \frac{e^{2K} - 1}{1 - \tilde{y}^2} d\tilde{y} + \int_0^y \frac{1}{1 - \tilde{y}^2} d\tilde{y} \right). \quad (54)$$

The choice of the integration constants ensures regularity of y_B , i.e. $\lim_{y \rightarrow \pm 1} y_B = \pm 1$ and for spacetimes with equatorial plane symmetry, y_B is symmetric as well. The conformal factor can be written as

$$\omega = \frac{2e^K}{(1+y)e^\Delta + (1-y)e^{-\Delta}}, \quad (55)$$

where

$$\Delta(y) = \frac{1}{2} \int_{-1}^y \frac{e^{2K} - 1}{1 - \tilde{y}^2} d\tilde{y} + \frac{1}{2} \int_1^y \frac{e^{2K} - 1}{1 - \tilde{y}^2} d\tilde{y}. \quad (56)$$

The regularity of the conformal factor can be directly seen if we write Eq. (56) as

$$\Delta(y) = \int_{-1}^y d\tilde{y} \int_0^1 d\alpha e^{2\alpha K} \hat{K} + \int_1^y d\tilde{y} \int_0^1 d\alpha e^{2\alpha K} \hat{K}, \quad (57)$$

where using Eq. (15) we have defined

$$\hat{K} = \frac{K}{\sin^2 \theta}. \quad (58)$$

III. THE NUMERICAL IMPLEMENTATION

We use an equidistant grid covering our numerical domain $(x, y) \in [0, 1] \times [-1, 1]$ with grid spacings $\Delta x = 1/N_x$, $\Delta y = 1/N_y$, where $N_x + 1$ is the number of grid points in the radial direction and $2N_y + 1$ is the number of grid points in the angular direction (N_y is the number of angular grid zones per hemisphere). All variables are defined on the grid $(u^n, x_i, y_j) = (n\Delta u, i\Delta x, j\Delta y)$, except for the quantities \hat{U} and τ which are defined on a staggered grid $(u^n, x_{i+1/2}, y_{j+1/2}) = (n\Delta u, (i+1/2)\Delta x, (j+1/2)\Delta y)$. As shown by [5] the use of a staggered grid is necessary for stability.

A. The fluid evolution

In our implementation of the fluid equations we closely follow the work of Papadopoulos and Font [10]. The hyperbolic mathematical character of the hydrodynamic equations allows for a solution procedure based on the computation of (local) Riemann problems at each cell-interface of the numerical grid. At cell i, j the state-vector \mathbf{U} is updated in time (from u^n to u^{n+1}) using a conservative algorithm

$$\begin{aligned} \mathbf{U}_{i,j}^{n+1} = \mathbf{U}_{i,j}^n & - \frac{\Delta u}{\Delta x} (\hat{\mathbf{F}}_{i+1/2,j} - \hat{\mathbf{F}}_{i-1/2,j}) \\ & - \frac{\Delta u}{\Delta y} (\hat{\mathbf{G}}_{i,j+1/2} - \hat{\mathbf{G}}_{i,j-1/2}) \\ & + \Delta u \mathbf{S}_{i,j}, \end{aligned} \quad (59)$$

where the numerical fluxes, $\hat{\mathbf{F}}$ and $\hat{\mathbf{G}}$, are evaluated at the cell interfaces according to some particular *flux-formula*

which makes explicit use of the full spectral decomposition of the system. For our particular formulation of the hydrodynamic equations such characteristic information was presented in [10]. We note that unlike in previous work [14], we have now included the metric determinant in the definition of the conserved quantities \mathbf{U} . Nevertheless, as was explicitly demonstrated in [28], the eigenvalues needed for the computation of the local Riemann problems remain unchanged.

In more precise terms the hydrodynamics solver of our code uses a second order Godunov-type algorithm, based on piecewise linear reconstruction procedures at each cell-interface [32, 33] and for simplicity the HLLC approximate Riemann solver [34, 35]. For the time update we use the second order Runge-Kutta algorithm derived in [36]. General information on HRSC schemes in relativistic hydrodynamics can be found, e.g. in [11, 37] and references therein.

We use the procedure described in [28] to explicitly recover the physical (primitive) variables for the perfect fluid EoS $p = (\Gamma - 1)\rho\epsilon$, Γ being the adiabatic index of the fluid. We solve for the primitive variables ϵ , ρ , u^x and u_y and then use the normalization condition to determine u^u .

B. The metric evolution

For the time update of the metric field $\hat{\gamma}$, we solve the wave equation (22) with a so-called *parallelogram algorithm*, based on a parallelogram consisting of ingoing and outgoing characteristics [4, 5, 38]. We closely follow the implementation of [5] to which the reader is referred for more details. In contrast to this work, however, we only use a single form of the wave equation in our numerical implementation, which is regular at \mathcal{J}^+ . This regularization is accomplished by rewriting the parallelogram identity in terms of the quantity

$$\Phi = \hat{\psi} f. \quad (60)$$

Explicitly, for a parallelogram Σ with left upper corner P , right upper corner Q , left lower corner R and right lower corner S (see Fig. 1) the algorithm reduces to

$$\begin{aligned} \Phi_Q &= \frac{1}{4} \Delta u r_Q f|_Q \hat{H}_c \\ &+ \frac{f|_Q}{f|_P} (\Phi_P - \frac{1}{4} \Delta u r_P f|_P \hat{H}_c) \\ &+ \frac{f|_Q}{f|_S} (\Phi_S + \frac{1}{4} \Delta u r_S f|_S \hat{H}_c) \\ &- \frac{f|_Q}{f|_R} (\Phi_R + \frac{1}{4} \Delta u r_R f|_R \hat{H}_c). \end{aligned} \quad (61)$$

In the above expression \hat{H}_c denotes the source term of Eq. (25) at the center of the parallelogram approximated to second order accuracy. The regularity of this expres-

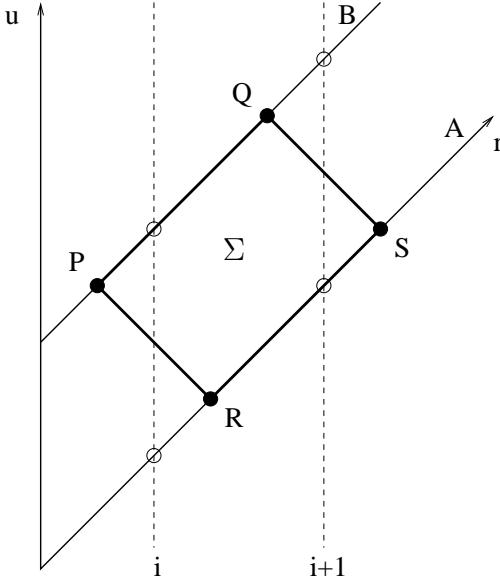


FIG. 1: Parallelogram $PQRS$ consisting of ingoing and outgoing light cones. We have displayed the outgoing light cones at two different coordinate values u , A and B , foliating our spacetime. For simplicity, all null lines have angles 45° . In addition to the parallelogram we have marked radial grid points at i and $i+1$.

sion can be easily seen for our compactified grids

$$r(x) = a \frac{x}{1-x^b}, \quad b \geq 1, \quad (62)$$

as

$$rf = \sqrt{a} \frac{x}{\sqrt{1+(b-1)x^b}} \quad (63)$$

and

$$\frac{f|_Q}{f|_S} = \frac{1-x_Q}{1-x_S} \frac{\sum_{i=0}^{b-1} x_Q^i}{\sum_{j=0}^{b-1} x_S^j} \frac{\sqrt{1+(b-1)x_P^b}}{\sqrt{1+(b-1)x_Q^b}}. \quad (64)$$

All the terms on the right hand side of Eq. (64) are explicitly regular for $x \rightarrow 1$ ($r \rightarrow \infty$), except for the first factor which is regular according to the discussion in [5].

We discretize the hypersurface equation (17) (and similarly Eq. (19)) as

$$\beta_{i,j} = \beta_{i-1,j} + \mathcal{H}_{\beta_{i-1/2,j}} \Delta x, \quad (65)$$

where \mathcal{H}_β denotes the right hand side of Eq. (17). To solve the hypersurface equation (18), we discretize the alternative equation

$$2xf \left(r^4 f^4 \hat{U}_x \right)_{,x^4} + r^2 f^2 \left(-\frac{1}{2} (f^2)_{,x} \frac{r^2}{x^2} f^2 \right)^{\frac{1}{2}} - \frac{r^2}{x^2} (f^2)^{\frac{3}{2}} (\beta_{,x} - \hat{\gamma}_{,x} \bar{y}) \hat{U}_{,x} = \frac{r^2}{x^2} f^3 e^{2(\beta - \bar{y} \hat{\gamma})} \mathcal{H}_u, \quad (66)$$

where the right hand side of Eq. (18) has been denoted by $2r^2 \mathcal{H}_u$. The derivative $\partial/\partial x^4 = \frac{1}{4x^3} \partial/\partial x$ was introduced to ensure regularity at the origin.

In the following, we describe the order of the time update from light-cone A at time u to light-cone B at time $u + \Delta u$ (see Fig. 1). Let us assume that we know the primitive and conserved fluid variables, and the metric quantities $\hat{\gamma}$, β , \hat{U} and S on the light cone A . In a first step we globally determine the conserved fluid variables on B . For the metric update, in contrast, we march from the origin to the exterior of the light-cone B . Having previously obtained the variables up to grid point i (either from the specific boundary treatment at the origin or during the marching process), we first determine $\hat{\gamma}$ at grid point $i+1$. In a second step we solve for β , \hat{U} and S at $i+1$ in that particular order, recovering the primitive variables with the metric thus obtained. As the hypersurface integration for the metric depends on the primitive variables at the grid point to be determined, we iterate the hypersurface and recovery algorithm until convergence.

In order to obtain stability in our explicit algorithms when solving the fluid and metric equations we have to fulfill the Courant-Friedrichs-Levy condition - the numerical domain of dependence must include the analytical domain of dependence. This limits the maximal time step allowed in each time update. Calculating the characteristic speeds for the fluid system, the fluid update sets a limit on the time step as

$$\Delta u \leq \min(c_1 \Delta x, c_2 \Delta y), \quad (67)$$

where c_1 and c_2 are constants and the minimum is calculated for the entire fluid grid. For the metric update, it can be shown that the evolution near the origin sets the stricter theoretical limit

$$\Delta u = c_3 \Delta r (\Delta y)^2, \quad (68)$$

with $c_3 = 0.5$. In numerical experiments we found, however, that with our coupled code $c_3 \approx 10$, in good agreement with the result $c_3 = 8$ reported in [27]. With this result the time step restriction from Eq. (68) is not much stronger than the time step restriction from Eq. (67), at least for the angular resolutions we can afford. In the simulations described in this paper we use time steps of 0.6 times the maximal time step consistent with the fluid evolution Eq. (67). With this procedure, it was not necessary to implement implicit methods for the metric update.

As for the vacuum equations the origin of coordinates, where we assume that the coordinate system is a local Fermi system, needs special care. The main change in the falloff behavior of the metric variables due to the presence of the fluid is in β . We impose a falloff behavior of the metric field $\hat{\gamma}$ as

$$\hat{\gamma} = a r^2 + b r^3, \quad (69)$$

where a and b are constants. At the origin the radial dependence of β is $\beta = O(r^2)$, instead of $\beta = O(r^4)$ for

the vacuum case (from Eq. (17)). To ensure regularity of the fluid at the origin, we have to impose [3]

$$u_r = D + Ey + O(r), \quad (70)$$

$$u_y = Er + O(r^2), \quad (71)$$

where D and E fulfill $-D^2 + E^2 = -1$. With the definitions (the leading terms can be extracted from the hypersurface equations)

$$\beta = \frac{r^2}{8}\kappa\rho h(D + Ey)^2 + F(y)r^3, \quad (72)$$

$$\hat{U} = 4y(ar + \frac{3}{5}br^2) + \frac{1}{2}\kappa\rho h(D + Ey)Er + C(y)r^2, \quad (73)$$

$$\kappa\rho hu_y u_y = \kappa\rho hE^2 r^2 + G(y)r^3, \quad (74)$$

the quadratic terms in r in the wave equation reduce to an equation for a

$$a_{,u} = \frac{6}{5}b - \frac{1}{3}C_{,y} + \frac{1}{6}F_{,yy} + \frac{1}{12}G. \quad (75)$$

(In the absence of matter this reduces to $a_{,u} = \frac{6}{5}b$, see [5]). We extract a , b , C , F and G at the old time slice and then solve Eq. (75) to obtain a at the new time slice. Inserting this value into the leading order in r of Eq. (69) and Eq. (73), we calculate $\hat{\gamma}$ and \hat{U} at the two first grid points, which then allows us to start the marching algorithms described above for the metric update.

In our numerical implementation we use a standard second order integration for the double integrals in Eq. (57) and we determine the conformal factor according to Eq. (55) afterwards. Furthermore, to solve the hypersurface equations for the auxiliary variables τ and μ (μ is needed for the Bondi mass, Eq. (44)), we also use a second order discretization. By simply reading off the metric values at \mathcal{J}^+ , it is finally possible to determine the Bondi mass and news.

IV. CODE TESTS

In order to validate the accuracy of our numerical code we have performed various tests aimed to check the different regimes of the implementation.

A. Spherically symmetric tests

In this section we describe tests of our code in dealing with spherically symmetric stellar models. In order to set up equilibrium models for relativistic stars we solve the Tolman-Oppenheimer-Volkoff equations in outgoing null coordinates [10]

$$p_{,r} = \left(\frac{1}{2r} - \frac{1}{2Y}(1 + 8\pi r^2 p) \right) \rho h, \quad (76)$$

$$Y_{,r} = 1 + 8\pi r^2(p - \rho h), \quad (77)$$

where $Y = Ve^{-2\beta}$. Moreover, for the study of oscillations of these spherical stellar models discussed below, we give some additional fluid perturbation. In order to obtain consistent initial data, we have to solve the hypersurface equations (7)-(9) imposing the normalization condition for the fluid. As we have presented results for a similar code elsewhere [14], we keep the presentation of this section short.

1. Stable relativistic stars

First we study equilibrium models of relativistic stars. In order to obtain initial data we solve the TOV equations (76)-(77) for a polytropic EoS $p = K\rho^\Gamma$, K being the polytropic constant. With complete initial data at hand we evolve stable equilibrium configurations in time. Both, for finite grids which only cover the star, as well as for compactified grids, where we cover the star and its entire exterior spacetime, we are able to maintain the initial equilibrium profiles of the star during a time-dependent simulation, for times much longer than the light-crossing time. Due to the discretization error, the stars are exited to oscillate in their radial modes of pulsations (see [14] for more details). Deviations from equilibrium converge to zero with increasing resolution with a second order convergence rate.

2. Migration of an unstable relativistic star

Following [39] we have checked the code on the dynamical evolution of an unstable spherical star. In such a model the sign of the truncation error of the numerical scheme controls the fate of the evolution: the star may either expand or collapse. In our code this sign is such that the unstable star “migrates” to the stable branch of the sequence of equilibrium models. In such a situation, the rest-mass of the star has to be conserved throughout the evolution. Despite being an academic problem this simulation represents an important test of the accuracy and self-consistency of the code in a highly dynamical situation.

As in [39] we have constructed a $n = 1$ ($\Gamma = 1 + 1/n = 2$), $K = 100$ polytropic star with mass $M = 1.447 M_\odot$ and central rest-mass density $\rho_c = 8.0 \times 10^{-3}$ (in units in which $G = c = M_\odot = 1$). As the radius of the star strongly increases during the evolution, we surround the star by a low density atmosphere. In order to avoid numerical problems in these zones we reset the fluid variables to their original atmosphere values once they have fallen below a threshold value (see [40] for more details). This artificial resetting enables the star to expand and to contract. Despite the use of an atmosphere the energy conservation properties are well satisfied [14].

Fig. 2 shows the evolution of the central density up to a final time of $u_B = 10$ ms. On a very short dynamical timescale the star rapidly expands and its cen-

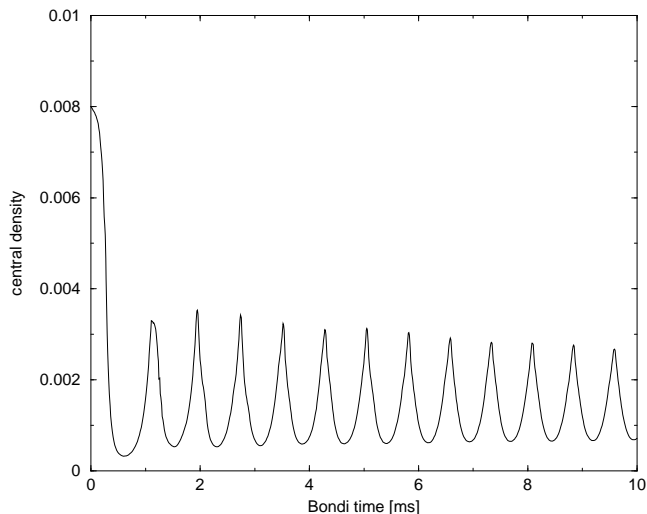


FIG. 2: Evolution of the central rest-mass density during the migration of an unstable relativistic star ($n = 1, K = 100, M = 1.447M_\odot, \rho_c = 8.0 \times 10^{-3}; G = c = M_\odot = 1$) to a stable model with the same rest-mass. The central density of the (final) stable configuration is $\rho_c = 1.35 \times 10^{-3}$. The evolution shows the expected behavior. Since we are using a polytropic EoS, the amplitude of the oscillations is essentially undamped for the evolution times shown.

tral rest-mass density drops well below its initial value, less than $\rho_c = 1.35 \times 10^{-3}$, the central rest-mass density of the stable model of the same rest-mass. During the rapid decrease of the central density, the star acquires a large radial momentum. The star then enters a phase of large amplitude radial oscillations around the stable equilibrium model. As Fig. 2 shows the code is able to accurately recover (asymptotically) the expected values of the stable model. Furthermore, the displayed evolution is completely similar to that obtained with an independent fully three-dimensional code in Cartesian coordinates [39].

The evolution shown in Fig. 2 allows to study large amplitude oscillations of relativistic stars, which could occur after a supernova core-collapse [41] or after an accretion-induced collapse of a white dwarf.

B. Tests beyond spherical symmetry

To the best of our knowledge we do not know of any regular exact (analytic) solution of the Einstein equations in axisymmetry with a non-vanishing perfect fluid matter field. However, there is an exact solution for the vacuum equations which was already used to check the vacuum code of [5]. As we have generalized the coordinate system, we use here the same solution to check our code.

In addition, to test the overall implementation of the code we examine the global conservation properties which can be rigorously established due to the compactification

of spacetime.

1. Exact vacuum solution SIMPLE

Following the work of [5] the metric

$$e^\gamma = \frac{1}{2}(1 + \Sigma), \quad (78)$$

$$e^{2\beta} = \frac{(1 + \Sigma)^2}{4\Sigma}, \quad (79)$$

$$U = -\frac{a^2 g \cos \theta}{\Sigma}, \quad (80)$$

$$V = \frac{r}{\Sigma}(2a^2 g^2 - a^2 r^2 + 1), \quad (81)$$

is a solution of the vacuum field equations for

$$\Sigma = \sqrt{1 + a^2 g^2}, \quad (82)$$

$$g = r \sin \theta, \quad (83)$$

where a is a constant. Using this solution with a suitable L2-norm to measure deviations we have checked that our metric solver is second order convergent.

2. Global energy conservation test

In this section we focus on a global energy conservation test. Starting with the equilibrium model of a neutron star (see next section for more details), we use a strong gravitational wave to perturb the star,

$$\hat{\gamma} = 0.2 e^{-3(r-4)^2} y. \quad (84)$$

Such a large amplitude is not realistic, but we choose it to test our numerical implementation in the nonlinear regime. Fig. 3 shows a contour plot of the initial gravitational wave shear. In what follows we use a radial grid with $r = 3 \frac{x}{1-x}$.

Fig. 4 shows the deviation from global energy conservation (see Eq. (52)) as a function of the grid resolution (circles) and the total energy radiated away in gravitational waves. The deviations from exact energy conservation converge to zero which represents a very severe global test for our numerical implementation.

There are two additional consistency conditions, which relate the metric quantities on \mathcal{J}^+ . These are [27]

$$S - U_{,\theta} - U \cot \theta = 0, \quad (85)$$

$$\gamma_{,u} + \frac{1}{2} e^{-2\gamma} \sin \theta \left(e^{2\gamma} \frac{U}{\sin \theta} \right)_{,\theta} = 0. \quad (86)$$

Our code reproduces these conditions, the errors converging to zero with a convergence rate of 1. Fig. 5 shows the deviation from zero for the first condition, thus checking the leading term in the falloff behavior of the quantity S at \mathcal{J}^+ .

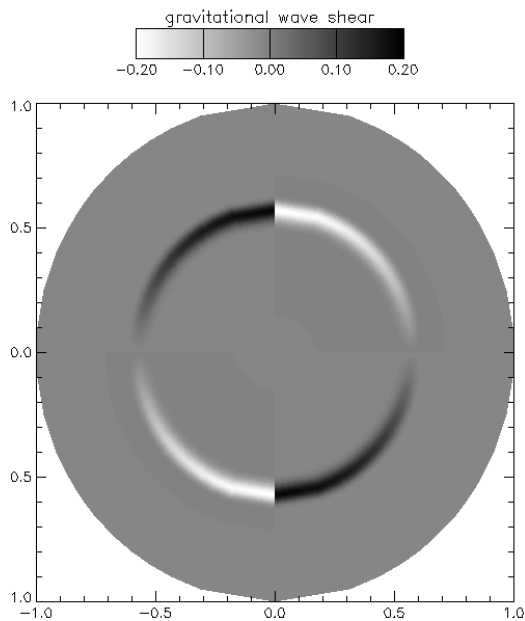


FIG. 3: Contour plot of the initial gravitational wave shear $\hat{\gamma}$, Eq. (84). The axes labels denote the value of the radial coordinate x along the equator (horizontal axis) and the symmetry axis (vertical axis), and they run from the origin of the coordinate system at $x = 0$ to future null infinity \mathcal{J}^+ at $x = 1$. The numerical domain comprises the half circle to the right of the vertical line at $x = 0$ (the symmetry axis), the left half is obtained from axisymmetry. The gravitational wave shear perturbation is located in a small ring at radius $r \approx 4$.

The obtained first-order convergence rate can be explained by the use of a *total variation diminishing* HRSC scheme for the fluid evolution, which, although it is second-order accurate in smooth, monotonous parts of the flow, reduces to first-order at local extrema, which are present in the interior of the numerical domain in this test (see [22] for alternative *essentially nonoscillatory* schemes). Tests including propagation and scattering off the origin of pure vacuum gravitational fields yielded the expected second-order convergence.

V. PULSATIONS OF RELATIVISTIC STARS

Oscillations of neutron stars, although believed to emit only weak gravitational waves (at least in the absence of instabilities) are interesting sources for future gravitational wave detectors (for a recent review see [42]).

In this section we apply our code to the study of axisymmetric pulsations of relativistic stars. We focus our analysis on one specific stellar model. We choose a relativistic polytrope $p = K\rho^{1+\frac{1}{n}}$ with polytropic index $n = 1$, polytropic constants $K = 100$ and central density $\rho_c = 1.28 \times 10^{-3}$ (in units in which $c = M_\odot = G = 1$). This model, which has a total mass of $M = 1.4M_\odot$ has already been used in previous work [22, 23, 39], which al-

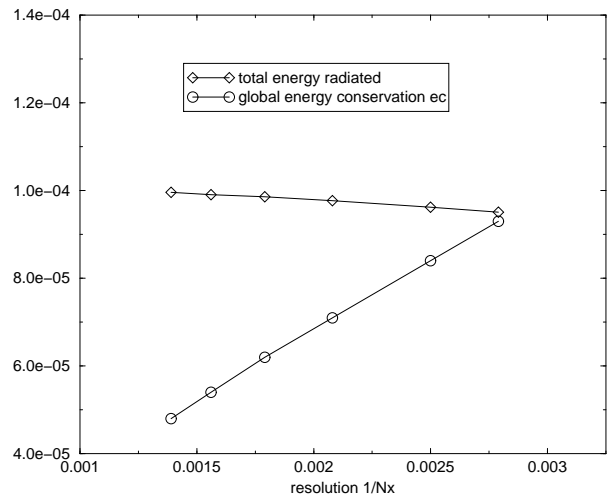


FIG. 4: Global energy conservation test for a neutron star and a strong gravitational wave. Plotted are the deviation from global energy conservation ec (circles, see Eq. (52)) and the total energy emitted by gravitational waves as a function of the grid resolution. The final integration time is $u_B = 2 \cdot 10^{-8}$ s, the total number of angular grid points $2N_y = 0.1N_x$.

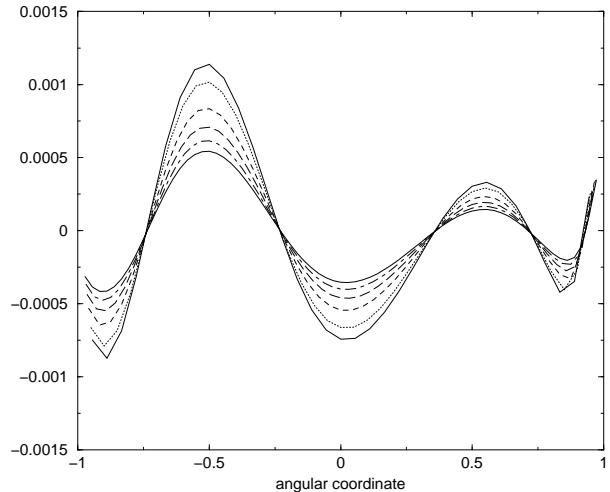


FIG. 5: Consistency check for the global norm Eq. (85) at \mathcal{J}^+ . Plotted are deviations from zero as a function of the angular coordinate y and for the same resolutions used in Fig. 4. The errors decrease with resolution, the convergence rate is one.

lows us to compare our results for the radial frequencies and fixed background evolutions in axisymmetry.

A. The perturbations

In order to excite the radial oscillation modes of the star ($l = 0$) we perturb the equilibrium configuration

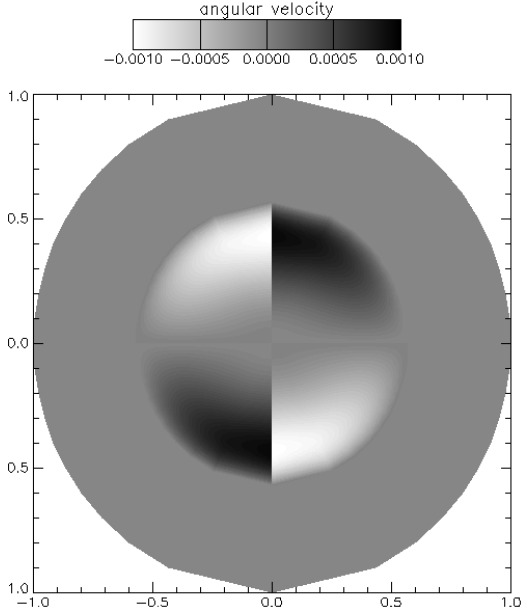


FIG. 6: Contour plot of the angular velocity perturbation u_y , Eq. (90). The axes labels denote the value of the radial coordinate x along the equator (horizontal axis) and the symmetry axis (vertical axis), and run from the origin of the coordinate system at $x = 0$ to future null infinity \mathcal{J}^+ at $x = 1$. The star corresponds to the inner circle, where the velocity perturbations are non-zero, with the north pole above.

using the perturbation

$$\delta\rho = A\rho_c \sin\left(\frac{\pi r^2}{R^2}\right), \quad (87)$$

$$\delta p = \left(1 + \frac{1}{n}\right)p\frac{\delta\rho}{\rho}, \quad (88)$$

where A is the amplitude of the perturbation.

Additionally, to excite the $l = 1, 2$ non-radial modes we perturb the angular velocity component according to

$$u_y = A \sin\left(\frac{\pi r^2}{R^2}\right), \quad (89)$$

$$u_y = A \sin\left(\frac{\pi r^2}{R^2}\right) \cos\theta, \quad (90)$$

respectively. Fig. 6 shows the initial setup and a contour plot of the perturbation given by Eq. (90).

Following [22, 23], in order to determine the different oscillation modes, we analyze the time evolution of different (fluid and metric) variables at a fixed coordinate location. We have checked that the frequencies of the oscillation modes are largely independent of the specific location. Hence, for the results presented here, we have restricted ourselves to extracting those frequencies at coordinates $(x, y) = (\frac{\tilde{N}_x}{2}\Delta x, \frac{\tilde{N}_y}{2}\Delta y)$, where \tilde{N}_x denotes the number of radial zones covering the star. In addition we use a radial coordinate

$$r = 15 \frac{x}{1 - x^4}, \quad (91)$$

TABLE I: Mode frequencies obtained in the Cowling approximation for a relativistic polytrope with $K = 100$, $n = 1$ and central density $\rho_c = 1.28 \times 10^{-3}$ in units in which $c = G = M_\odot = 1$. The first column labels the different modes. The second column shows the frequencies obtained with our code, the third column the results obtained with a different nonlinear code based on Cauchy slices [23]. The fourth column indicates the frequencies obtained from a linear perturbation code [22] for the quadrupolar modes. The last column shows the relative difference between the present code and the results of [23] in percent.

Mode	Present	Code [23]	Perturbation [22]	Difference
	(kHz)	(kHz)	(kHz)	(per cent)
F	2.690	2.706	-	0.59
H_1	4.636	4.547	-	1.96
H_2	6.532	6.320	-	3.35
H_3	8.418	8.153	-	3.25
1f	1.388	1.335	-	3.97
1p_1	3.504	3.473	-	0.89
1p_2	5.510	5.335	-	3.28
1p_3	7.400	7.136	-	3.70
2f	1.871	1.852	1.884	1.03
2p_1	4.143	4.100	4.110	1.05
2p_2	6.135	6.019	6.035	1.93
2p_3	8.087	7.867	7.873	2.80

and we choose a perturbation amplitude of $A = 10^{-3}$. We focus on the time evolution of the radial velocity u^x for the extraction of radial modes and on the angular velocity u_y for the extraction of non-radial modes. The calculation of mode frequencies follows the work of [23], i.e. we determine the zeros of the first derivative of the Fourier transform. These zeros correspond to maxima in the Fourier transform which are associated with the excited modes of oscillation.

B. Fixed background evolutions

We start presenting the results for the mode frequencies of the above stellar model obtained in evolutions in which we fix the background geometry of the spacetime (i.e. we adopt the so-called Cowling approximation). We compare the results to the literature, thus testing the hydrodynamics solver of our code.

Table I shows the results for the fundamental radial mode (F) and the first three overtones ($H_1 - H_3$) and the f and p modes for both, the $l = 1$ and $l = 2$ perturbation. Our results are in good agreement with both, a different nonlinear code [23] and an independent linear code based upon perturbation theory [22]. There are several reasons which explain the observed differences: First, the grid resolution used in our simulations is rather low (451×21 grid points in x and y , respectively) compared

to the finer grids used in [23] (200×80), especially in the angular direction. For the current setup - in contrast to [23] - only about one half of the radial zones is used to cover the star. We note that we use this choice here for comparisons with the results of the next section, where we also have to resolve gravitational waves in the exterior spacetime. Second, we have not implemented an atmosphere surrounding the star in a few zones as in [23], which enables the star to radially contract and expand. Therefore, the surface of the star may be too rigid, which may affect the mode frequencies slightly. The numerical implementation of such an atmosphere, however, requires a problem-dependent adaptation of its parameters. Third, and perhaps most importantly, as described in Sec. III A we use a second order reconstruction scheme at the cell interfaces, and not the third order PPM scheme used in [23]. It is worth emphasizing the importance of using high-order schemes for the hydrodynamics in order to improve the frequency identification (see related discussion in [22]). Nevertheless, for our only purpose of assessing the validity of the code we think that the overall agreement found is satisfactory.

C. Metric-fluid coupled evolutions

In this section we extract the mode frequencies of the above stellar model from fully coupled evolutions of the fluid and the geometry.

Fig. 7 shows the (Bondi) time evolution of the radial velocity u^x for the $l = 0$ perturbation (top panel), as well as the Fourier transform of this quantity. In the same way, Figs. 8 and 9 display the angular velocity evolution u_y and the Fourier transform for the $l = 1$ and $l = 2$ perturbation, respectively.

The final evolution time in Figs. 7-9 corresponds to 5 ms. The distinctive oscillatory pattern depicted in these figures is mainly a superposition of the lowest-order normal modes of the fluid. The high-frequency modes are usually damped fast by the intrinsic viscosity of the numerical schemes and at late times the star mostly pulsates in its lowest frequency modes.

We summarize our results on the mode frequencies in Table II. Note that due to the conservation of linear momentum the 1f mode does not exist (see Fig. 8) [23]. As in the Cowling simulations of the previous section we also find now good agreement when comparing to results of an independent nonlinear code [39] and to results of linear perturbation theory [39, 43]. The reasons mentioned in the above section for the observed discrepancies are still valid here, together with the new source of error introduced by the metric evolution.

D. Gravitational waveform

To end the validation of our code we study the gravitational wave signal from the simulations of the above

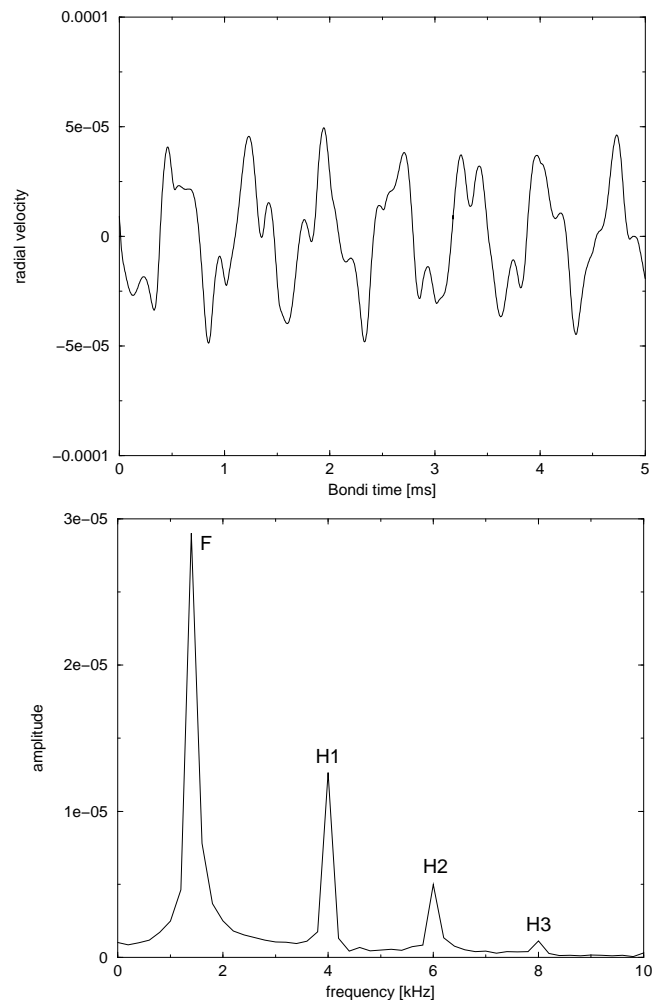


FIG. 7: Pulsations of a $K = 100, n = 1, \rho_c = 1.28 \times 10^{-3}$ polytrope ($c = G = M_\odot = 1$). Top panel: Time evolution of the radial velocity u^x for the $l = 0$ perturbation. Bottom panel: Fourier transform of the radial velocity. We have labeled the different oscillation modes, F (fundamental) and $H_1 - H_3$ (first three overtones).

section concerning the $l = 2$ perturbation. In Fig. 10 we plot the Bondi news function at the equator $N(y_B = 0)$ as a function of the observer time. Due to the equatorial plane symmetry inherent to the perturbation, which is conserved during the evolution, we have $y_B(y = 0) = 0$, which enables us to directly plot $N(y = 0)$, thus avoiding suitable interpolations for the wave extraction.

In order to estimate the amplitude of the signal in Fig. 10 we have also computed the gravitational wave emission due to the quadrupole formula. In the light-cone approach, the *quadrupole news* takes the form [44]

$$N_0 = \ddot{Q}. \quad (92)$$

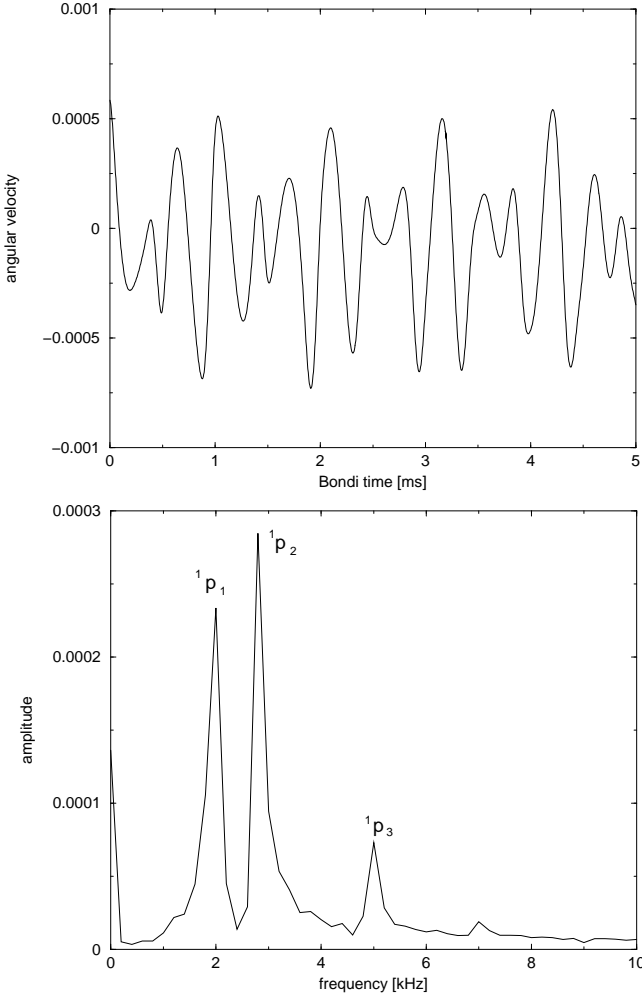


FIG. 8: Pulsations of a $K = 100, n = 1, \rho_c = 1.28 \times 10^{-3}$ polytrope ($c = G = M_\odot = 1$). Top panel: Time evolution of the angular velocity u_y for the $l = 1$ perturbation. Bottom panel: Fourier transform of the angular velocity.

The relevant quadrupole moment in axisymmetry reads

$$Q = \pi \sin^2 \theta \int_0^R dr' \int_0^\pi \sin \theta' d\theta' r'^4 \rho(1+\epsilon) \left(\frac{3}{2} \cos^2 \theta' - \frac{1}{2} \right). \quad (93)$$

We have included the factor $(1+\epsilon)$ in the formula to account for the relativistic internal energy. In the numerical calculation of Q we equate the radial and angular coordinates r' and θ' with the radial and angular coordinates r and θ . It is well known [45] that the three time derivatives in Eq. (92) can cause severe numerical error. In order to avoid this problem we fit a cosine to the time evolution of the quadrupole moment Q obtained in the numerical simulation. The dashed line in Fig. 10 shows the third time derivative of this curve, where the time derivatives are taken with respect to Bondi time.

By evaluating the contributions of the gravitational wave signal in Fig. 10, we see that the dominant contribution originates from the 2f mode. The frequency we

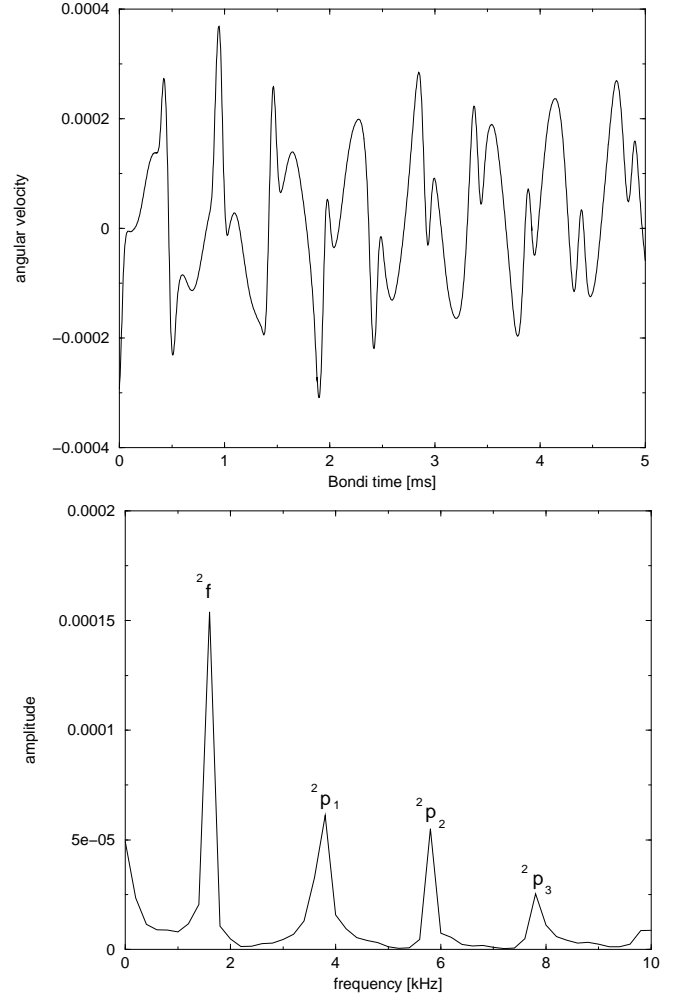


FIG. 9: Pulsations of a $K = 100, n = 1, \rho_c = 1.28 \times 10^{-3}$ polytrope ($c = G = M_\odot = 1$). Top panel: Time evolution of the angular velocity u_y for the $l = 2$ perturbation. Bottom panel: Fourier transform of the angular velocity.

extract from the waveform is 1.57 kHz, in good agreement with the result shown in Table II. There are additional contributions to the gravitational wave signal. The excitation of the 1p_1 mode is created at the outer boundary of the fluid, where we do not allow the star to radially contract or to expand.

Comparing the amplitude of the Bondi news and the quadrupole news for the 2f mode we stress that the amplitude roughly agree. We cannot exclude that the differences are mainly due to numerical errors. Due to the different contributions of the time derivative for γ and gauge terms the calculation of N is a difficult task [30]. In addition, we note that the total energy radiated away for our setup corresponds only to a tiny fraction of the total mass of the spacetime. More precisely, whereas the total spacetime mass is $1.4M_\odot$, the total mass radiated is only $2.8 \times 10^{-9}M_\odot$, which is smaller than the typical numerical errors in the determination of the Bondi mass. Moreover, most of this radiation is a consequence

TABLE II: Mode frequencies obtained in the coupled evolution for the relativistic polytrope with $K = 100$, $n = 1$ and central density $\rho_c = 1.28 \times 10^{-3}$ in units in which $c = G = M_\odot = 1$. The first column labels the different modes. The second column shows the frequencies obtained with our code and the third column shows the results obtained from linear perturbation theory [39, 43]. The last column shows the deviations in percent.

Mode	Present Code (kHz)	Perturbation [39], [43] (kHz)	Difference (per cent)
F	1.422	1.442	1.38
H_1	3.993	3.955	0.96
H_2	6.021	5.916	1.77
H_3	7.968	7.776	2.46
1p_1	1.951	-	-
1p_2	2.844	-	-
1p_3	5.019	-	-
2f	1.587	1.579	0.51
2p_1	3.748	3.710	1.02
2p_2	5.811	5.689	2.14
2p_3	7.848	7.580	3.54

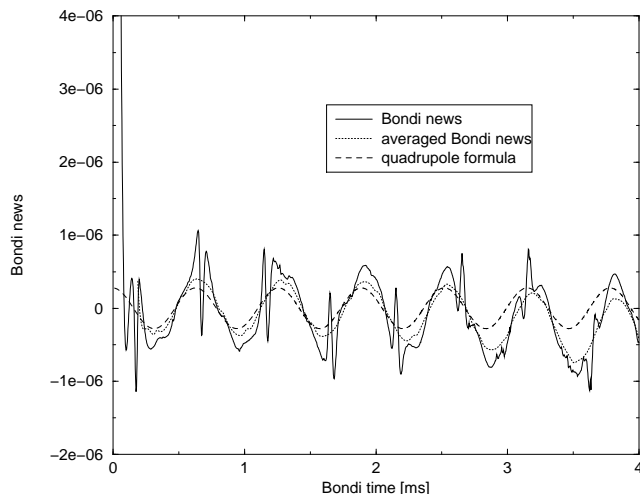


FIG. 10: News function as a function of observer time at infinity at the equator. The (unphysical) initial signal is due to the gravitational wave content in the initial data. The main oscillation frequency corresponds to the 2f mode with other frequencies overlayed. The dotted curve shows a suitable average of the numerical Bondi news smearing out higher frequencies. The dashed line corresponds to the estimated amplitude of the 2f mode oscillation which is extracted using the quadrupole formula. See text for a detailed discussion.

of the initial gravitational wave content and is radiated away in between $u_B = 0$ ms and $u_B = 0.1$ ms. Additional differences in the curves for the Bondi news and the quadrupole news in Fig. 10 might be created by the rough estimate of the quadrupole Q in Eq. (93) which

does not take into account the curvature of spacetime.

At late times (after about 3 ms), the Bondi news does not strictly oscillate around zero. This numerical effect can be weakened using more sophisticated numerical methods for the fluid update (e.g. third-order cell reconstruction procedures). We note that similar drifts are reported in [22, 39] in time evolutions of equilibrium models using a perfect fluid EoS. For the results shown in Fig. 10, we have used a polytropic EoS during the fluid evolution. This is legitimate as the effect of heating is negligible for our stellar object close to equilibrium. Finally, we note that the maximum deviation from global energy conservation, Eq. (52), in this simulation is $2.5 \times 10^{-5} M_\odot$, which is very adequate for the long integration time.

VI. CONCLUSION

We have presented numerical algorithms to solve the coupled Einstein-perfect fluid system in axisymmetry. Our approach is based upon the characteristic formulation of general relativity in which spacetime is foliated with a family of outgoing light cones emanating from a regular center. Due to a suitable compactification of the spacetime future null infinity is part of our finite numerical grid where we unambiguously extract gravitational waves.

Applying the nonlinear, fully relativistic code to studies of neutron stars modeled as polytropes, it has passed several tests, aimed at testing both the fluid evolution as well as the metric solver in the nonlinear regime. The code can accurately maintain long-term stability of relativistic stars and we have applied it to the study of stellar pulsations. We have extracted the frequencies of different non-radial fluid modes and the gravitational wave signal arising in time evolutions of perturbed stellar configurations. Applications of the present code in the computation of the gravitational waveforms emitted in axisymmetric core collapse situations will be presented elsewhere.

VII. ACKNOWLEDGEMENTS

It is a pleasure to thank Kostas Kokkotas, who calculated mode frequencies for us using his linear perturbation code. We also would like to thank Nick Stergioulas and Luis Lehner for helpful comments and discussions. This work has been supported in part by the EU Programme 'Improving the Human Research Potential and the Socio-Economic Knowledge Base', (Research Training Network Contract HPRN-CT-2000-00137). P.P. acknowledges support from the Nuffield Foundation (award NAL/00405/G). J.A.F acknowledges support from a Marie Curie fellowship from the European Union (MCFI-2001-00032).

-
- [1] C.R. Evans, in *Dynamical spacetimes and numerical relativity*, ed. J.M. Centrella, Cambridge Univ. Press (1986).
 - [2] R.F. Stark, T. Piran, Phys. Rev. Lett. **55**, 891-894 (1985).
 - [3] R.A. Isaacson, J.S. Welling, J. Winicour, J. Math. Phys. **24** 1824 (1983).
 - [4] R. Gómez, J. Winicour, R. Isaacson, J. Comp. Phys. **98** 11-25 (1992).
 - [5] R. Gómez, P. Papadopoulos, J. Winicour, J. Math. Phys. **35**(8) 4184-4204 (1994).
 - [6] P. Papadopoulos, gr-qc/0104024 (2001).
 - [7] R. Gómez, L. Lehner, P. Papadopoulos, J. Winicour, Class. Quant. Grav. **14** 4, 977-990 (1997).
 - [8] N. Bishop, R. Gómez, L. Lehner, M. Maharaj, J. Winicour, Phys. Rev. D **56** 6298-6309 (1997).
 - [9] R. Bartnik, A.H. Norton, SIAM J. Sci. Comput. **22**(3), 917-950 (2000).
 - [10] P. Papadopoulos, J.A. Font, Phys. Rev. D **61** 024015 (2000).
 - [11] J.A. Font, Living Reviews in Relativity **3** 2 (2000).
 - [12] P. Papadopoulos, J.A. Font, Phys. Rev. D **63** 044016 (2001).
 - [13] F. Linke, J.A. Font, H.T. Janka, E. Müller, P. Papadopoulos, Astron. Astrophys. **376** 568-579 (2001).
 - [14] F. Siebel, J.A. Font, P. Papadopoulos, Phys. Rev. D, in press, gr-qc/0108006 (2001).
 - [15] N. Bishop, R. Gómez, L. Lehner, M. Maharaj, J. Winicour, Phys. Rev. D **60** 024005 (1999).
 - [16] H. Bondi, M.G.J. van der Burg, A.W.K. Metzner, Proc. Roy. Soc. A, **269** 21-52 (1962).
 - [17] R.K. Sachs, Proc. R. Soc. A **270** 103-126 (1962).
 - [18] L.A. Tamburino, J.H. Winicour, The Physical Review **150** 1039-1053 (1966).
 - [19] R. Penrose, Phys. Rev. Lett. **10** 2 66-68 (1963).
 - [20] R. Gómez, L. Lehner, R.L. Marsa, J. Winicour et al, Phys. Rev. Lett. **80** 3915-3918 (1998).
 - [21] J. Winicour, Living Reviews in Relativity **4** 3 (2001).
 - [22] J.A. Font, N. Stergioulas, K.D. Kokkotas, Mon. Not. R. Astron. Soc. **313** 678-688 (2000).
 - [23] J.A. Font, H. Dimmelmeier, A. Gupta, N. Stergioulas, Mon. Not. R. Astron. Soc. **325** 1463 (2001).
 - [24] M. Shibata, T.W. Baumgarte, S.L. Shapiro, Phys. Rev. D **61** 044012 (2000).
 - [25] M. Shibata, T.W. Baumgarte, S.L. Shapiro, Astrophys. J. **542** 453-463 (2000).
 - [26] N. Stergioulas, J.A. Font, Phys. Rev. Lett. **86**, 1148-1151 (2001).
 - [27] P. Papadopoulos, PhD thesis Univ. Pittsburgh (1993).
 - [28] P. Papadopoulos, J.A. Font, gr-qc/9912094 (1999).
 - [29] R. Gómez, J. Winicour, Phys. Rev. D **45**, 2776-2782 (1992).
 - [30] R.A. Isaacson, J.S. Welling, J. Winicour, Phys. Rev. Lett. **53** 20 (1984).
 - [31] R. Gómez, P. Reilly, J. Winicour, R. Isaacson, Phys. Rev. D **47**, 8 3292-3302 (1993).
 - [32] B. van Leer, J. Comp. Phys. **23** 276 (1977).
 - [33] B. van Leer, J. Comp. Phys. **32** 101 (1979).
 - [34] B. Einfeldt, SIAM J. Num. Anal. **25** 294 (1988).
 - [35] A. Harten, P.D. Lax, B. van Leer, SIAM Review **25**, 35 (1983).
 - [36] C.-W. Shu, S. Osher, J. Comp. Phys. **83**, 32-78 (1989).
 - [37] E. Müller, in *Computational Methods for Astrophysical Fluid Flow*, ed. O. Steiner, A. Gautschy, Springer (1998).
 - [38] J. Winicour, gr-qc/0003029 (2000).
 - [39] J.A. Font, T. Goodale, S. Iyer, M. Miller et al., Phys. Rev. D, in press, gr-qc/0110047 (2001).
 - [40] J.A. Font, M. Miller, W.-M. Suen, M. Tobias, Phys. Rev. D **61** 044011 (2000).
 - [41] H. Dimmelmeier, J.A. Font, E. Müller, Astrophys. J. **560**, L163-L166 (2001).
 - [42] K.D. Kokkotas, N. Andersson, gr-qc/0109054 (2001).
 - [43] K.D. Kokkotas, Private communication.
 - [44] J. Winicour, Gen. Rel. Grav. **19**, 3, 281-287 (1987).
 - [45] L.S. Finn, in *Frontiers in Numerical Relativity*, ed. C.R. Evans, L.S. Finn, D.W. Hobill, Cambridge Univ. Press (1989).